Effects of form-induced velocity in rough-wall turbulent channel flows

By S. C. Mangavelli and J. Yuan[†][‡]

Abstract

Wall roughness induces form-induced (or dispersive) velocity and pressure perturbations inside the roughness sublayer of a wall-bounded turbulent flow. This work discusses the role played by the form-induced velocity in influencing turbulence statistics and structure, using existing direct numerical simulation data of transient half channels in response to an impulse acceleration (Mangavelli *et al.*, *J. Turbul.*, **22**:434–460, 2021). Focuses are given to (i) reshaping of turbulent coherent motions by the rate-of-strain of the mean velocity, and (ii) contributions of different velocity sources to turbulent pressure fluctuations. Half-channel flows in both fully-developed and non-equilibrium, transient states are discussed. Results show that form-induced velocity gradients not only form an important source of turbulent pressure in an equilibrium flow, but also lead to turbulence production and potentially direct structural change of turbulent eddies in a non-equilibrium flow under acceleration.

1. Introduction

Wall roughness plays an important role in many fields of study. Much has been done to identify the effects of roughness on wall-bounded turbulence, equilibrium or non-equilibrium, with focuses on wall friction and statistics of mean flow and turbulence. See reviews provided by Raupach *et al.* (1991), Jiménez (2004), Chung *et al.* (2021), as well as Finnigan (2000) in atmospheric applications. In addition, recent reviews on current knowledge regarding rough-wall non-equilibrium turbulence were provided by Devenport & Lowe (2022) and Volino *et al.* (2022).

One approach to describe and quantify the dynamical effects of roughness on turbulence is to analyze changes in the governing equations due to the presence of roughness. As shown by Raupach & Shaw (1982), Mignot *et al.* (2009) and Yuan & Piomelli (2015), additional terms in the transport equations of linear momentum and Reynolds stresses appear with the presence of roughness when a double-averaging process is applied to the equations. This averaging process performs a triple decomposition of an instantaneous fluid variable $\theta(x, y, z, t)$, such that $\theta = \langle\overline{\theta}\rangle + \widetilde{\theta} + \theta'$, where $\overline{()}$ is time averaging for a steady problem (or ensemble averaging for an unsteady one), $()' = () - \overline{()}$ is turbulent fluctuation, and $\langle\rangle$ is intrinsic spatial averaging (i.e. value per unit fluid area) along homogeneous directions. $\widetilde{\theta} = \overline{\theta} - \langle\overline{\theta}\rangle$ is the spatial heterogeneity of the local averaged θ, called the dispersive or form-induced fluctuations. Superficial spatial averaging $\langle\cdot\rangle_s$ (i.e. fluid variable per unit total area) is also used. $\langle\overline{\theta}\rangle$ is the double-averaged (DA) value.

[†] Department of Mechanical Engineering, Michigan State University
[‡] Corresponding author. Email: junlin@egr.msu.edu

The DA linear momentum equation is

$$\frac{\partial\langle\overline{u_i}\rangle_s}{\partial t}+\frac{\partial}{\partial x_j}\langle\overline{u_i}\rangle_s\langle\overline{u_j}\rangle=-\frac{1}{\rho}\frac{\partial\langle\overline{p}\rangle_s}{\partial x_i}+\nu\frac{\partial^2\langle\overline{u_i}\rangle_s}{\partial {x_j}^2}-\frac{\partial\langle\overline{u_i'u_j'}\rangle_s}{\partial x_j}-\frac{\partial\langle\widetilde{u}_i\,\widetilde{u}_j\rangle_s}{\partial x_j}+f_i. \tag{1.1}$$

Roughness gives rise to two additional terms in Equation (1.1): the fourth term on the right-hand-side representing the momentum transfer due to form-induced stresses, $\langle\widetilde{u}_i\widetilde{u}_j\rangle_s$ (Nikora *et al.* (2001), also termed "dispersive stresses" by Wilson & Shaw (1977)), and a body force (f_i) representing the sum of local pressure drag and viscous stress imposed on the surface of roughness. These two terms are significant near the wall. The near-wall layer in which the form-induced stress is significant compared to the DA velocity is called the roughness sublayer (RSL) (Pokrajac *et al.* 2007). Jelly & Busse (2019) showed that both $\langle\widetilde{u}\,\widetilde{v}\rangle$ and $\langle\overline{u'v'}\rangle$, in opposite signs, contribute significantly to the mean momentum balance near the roughness crest for a Gaussian roughness. Mangavelli *et al.* (2021) showed that, although in a fully developed channel flow $\langle\widetilde{u}\,\widetilde{v}\rangle$ is much weaker than $\langle\overline{u'v'}\rangle$, in a transient channel flow the $\langle\widetilde{u}\,\widetilde{v}\rangle$ magnitude may exceed temporarily that of $\langle\overline{u'v'}\rangle$ below the roughness crest.

The DA equations of normal Reynolds stresses (considering a channel flow) can be written as (no summation over Greek index),

$$\begin{aligned}\frac{\partial\langle\overline{u_\alpha'^2}\rangle_s}{\partial t}=&\left[\underbrace{-2\langle\overline{u_\alpha'v'}\rangle_s\frac{\partial\langle\overline{u}_\alpha\rangle}{\partial y}}_{P_s}+\underbrace{P_w+P_m}_{P_s^f}\right]\underbrace{-\left\langle\frac{\partial}{\partial x_j}\widetilde{u_\alpha'u_\alpha'}\widetilde{u}_j\right\rangle_s}_{T_w}\underbrace{-\left\langle\frac{\partial}{\partial x_j}\overline{u_\alpha'u_\alpha'u_j'}\right\rangle_s}_{T_t}\\&\underbrace{-2\left\langle\overline{P'\frac{\partial u_\alpha'}{\partial x_\alpha}}\right\rangle_s}_{\Pi}\underbrace{-2\frac{\partial\langle\overline{P'u_\alpha'}\rangle_s}{\partial x_\alpha}}_{T_p}\underbrace{+\nu\left\langle\frac{\partial^2\overline{u_\alpha'^2}}{\partial x_j\partial x_j}\right\rangle_s}_{T_\nu}\underbrace{-2\nu\left\langle\overline{\frac{\partial u_\alpha'}{\partial x_j}\frac{\partial u_\alpha'}{\partial x_j}}\right\rangle_s}_{\epsilon},\end{aligned} \tag{1.2}$$

where the terms on the right-hand-side are, respectively, shear production due to double-averaged strain rates (P_s), additional shear production due to form-induced strain rates (P_s^f), additional transport due to form-induced velocities (T_w), turbulent transport (T_t), viscous transport (T_ν), pressure-strain-rate term (Π), pressure transport (T_p), and viscous dissipation (ϵ). Discussions on how the form-induced velocity modifies Reynolds-stress balance focused mainly on the P_s^f term, which represents conversion from the kinetic energy of the form-induced fluctuations at the roughness length scale (or "wake kinetic energy", WKE (Raupach & Shaw 1982)) to the turbulent kinetic energy (TKE) at smaller scales. The form-induced production was found to depend on the roughness geometry (Yuan & Aghaei-Jouybari 2018) and to play a more important role in Reynolds stress balance in non-equilibrium flows, such as in spatially accelerating boundary layers (Yuan & Piomelli 2015), oscillatory channel (Ghodke & Apte 2016) and transient accelerating channels (Mangavelli *et al.* 2021), than in canonical flows (Mignot *et al.* 2009; Yuan & Piomelli 2014*c*). In these studies, T_w was found to be small in comparison to other terms.

Besides TKE production, another key process that controls the development of turbulence is the distribution of TKE among velocity fluctuations in different directions, represented by the pressure strain term in Equation (1.2) and partially controlled by local p' intensity. It is not yet clear whether and how form-induced velocity modifies turbulent pressure and TKE redistribution.

Rough-wall turbulent flows in engineering applications such as those over naval vessels or airfoils/hydrofoils usually display temporal and/or spatial variations due to external factors including freestream pressure gradient, surface curvature, and flow unsteadiness. These flows are termed non-equilibrium if a similarity solution of velocity cannot be found. One type of non-equilibrium turbulence widely studied is the one under acceleration (or favorable longitudinal pressure gradient, FPG). Studies on smooth walls showed that a strong freestream acceleration causes the boundary layer to undergo reverse transition from a fully turbulent state to a quasi-laminar state (Narasimha & Sreenivasan 1973). This was attributed to the stretching of near-wall turbulent eddies, leading to elongated velocity streaks, quasi-one-dimensional turbulence, reduced TKE redistribution, and consequently stabilized turbulence, whose intensity decouples from the accelerated mean flow (Bourassa & Thomas 2009; Piomelli & Yuan 2013; Volino 2020). Roughness acts to counter the stabilizing effects of FPG (Cal *et al.* 2009; Yuan & Piomelli 2015), as it augments near-wall TKE and leads to a more isotropic Reynolds stress tensor.

Transient accelerated flows were shown to be fundamentally similar to those that undergo spatial acceleration. Based on DNS, He & Seddighi (2013) and Seddighi *et al.* (2015) characterized the response of turbulent channel flows to an impulse-like increase in flow rate, over smooth and rough walls. On the smooth wall, they observed similar flow response as that in a FPG boundary layer undergoing reverse transition: elongated low-speed streaks, laminar-like mean velocity profiles, higher Reynolds stress anisotropy, and a frozen pressure strain term. In the presence of pyramid roughness, such reverse transition was prevented. Based on DNS of transient half-channel flows with a similar configuration, Mangavelli *et al.* (2021) characterized how two different roughnesses with similar average and root-mean-square heights but different geometries affect the evolutions of mean and turbulent statistics. $\widetilde{u}_i$ in the RSL was observed to stay quasi-equilibrium (scaling with the velocity at the edge of the sublayer) throughout the transient process, in stark contrast to the non-equilibrium variation of u_i'. Strong form-induced production of TKE in all u_i' components contributes to a much faster recovery of the steady state on rough walls than on the smooth wall. The roughness geometry determines how fast turbulence recovers to the steady state.

The description above summarizes the current knowledge on how roughness, as well as the $\widetilde{u}_i$ fields it induces, dynamically affects equilibrium and non-equilibrium wall-bounded turbulent flows. However, a few questions are still unanswered. One is whether form-induced velocity meaningfully affects Reynolds stress balance in a way other than additional TKE production, for example in modifying turbulent pressure and TKE redistribution. In addition, most previous attention were given to effects on turbulent statistics. Does $\widetilde{u}_i$ also contribute to different characteristics of turbulent structure observed on different rough walls?

2. Objectives

This work investigates the above questions in equilibrium and non-equilibrium channel flows, based on existing DNS data (Mangavelli *et al.* 2021) of transient half-channel flows subject to impulse accelerations on a smooth wall and two rough walls: a homogeneous, densely distributed sandgrain roughness and an inhomogeneous, multiscale roughness obtained from a hydraulic turbine scan. Mangavelli *et al.* (2021) focused on the development of turbulent statistics, while the present work extends the analyses to turbulent structure and various pathways through which $\widetilde{u}_i$ affects turbulence.

The organization of the rest of the manuscript is as follows. In Sec. 3, simulation

Case	Re_{b0}	$Re_{\tau 0}$	$k^+_{s\infty,0}$	$(\Delta x^+, \Delta z^+)_0$	Re_{b1}	$Re_{\tau 1}$	$k^+_{s\infty,1}$	$(\Delta x^+, \Delta z^+)_1$
SM	4,000	244	0	(4.0, 2.0)	12,000	626	0	(9.8, 4.8)
S	4,000	320	21	(5.0, 2.5)	12,000	1023	76	(15.3, 7.6)
T	4,000	294	10	(3.4, 3.4)	12,000	858	23	(10.1, 10.1)

Table 1: Simulation parameters at initial ('0') and new ('1') steady states. '+' indicates normalization in wall units (i.e. u_τ and viscous length scale $\delta_\nu = \nu/u_\tau$). Δx_i is the cell size in x_i direction. $Re_b = u_b\delta/\nu$ and $Re_\tau = u_\tau\delta/\nu$. δ is channel half height.

methodologies and parameters are described; statistical comparisons of the flow are also summarized. Then, two-point velocity correlations and spectra are compared in both steady and transient states in Sec. 5.1. To provide an explanation to the structural difference, the rate-of-strain tensor of $\widetilde{u}_i$ is characterized in Sec. 5.2. The velocity sources of the turbulent pressure are compared in Sec. 5.3 to evaluate the effects of $\langle\overline{u_i}\rangle$, $\widetilde{u}_i$ and u_i' on pressure fluctuations. Conclusions are provided in Sec. 6.

3. Problem fomulation

A summary of the methodologies and simulation setups as reported in Mangavelli *et al.* (2021) is provided here. The readers are referred to that publication for further details.

The incompressible flow of a Newtonian fluid was simulated by solving the equations of conservation of mass and momentum. x, y and z are, respectively, the streamwise, wall-normal and spanwise directions of the half-channel flow, and u, v and w are the velocity components in those directions. p is the pressure, ρ is the density and ν is the kinematic viscosity. Periodic boundary conditions are applied in x and z domain boundaries, and symmetric and no-slip conditions are applied to the top and bottom boundaries, respectively. In the rough cases, an immersed boundary method was used to impose the no-slip and no-penetration boundary condition on the rough walls. It is based on the volume-of-fluid approach; its detailed implementation in the in-house fluid solver was described by Yuan & Piomelli (2014*c*) and Yuan & Piomelli (2014*b*). The governing equations were solved on a staggered grid using second-order central differences for all terms, second-order accurate Adams-Bashforth semi-implicit time advancement, and Message-Passing Interface parallelization.

To conduct the present transient channel simulations, first a separate simulation was carried out for each case at the initial steady state with a bulk Reynolds number Re_{b0}, to generate statistics at this state and be used as initial conditions for the transient simulations. The transient simulations were then carried out, based on independent initial conditions, for around 20 times for each case to collect data for ensemble averaging at each time t. During a transient simulation, the variation of $Re_b(t)$ was imposed, equivalent to a rapid three-fold linear increase of the bulk velocity (u_b) that started at time $t = 0$ and lasted for a duration of $t^* = tu_{b0}/\delta = 0.08$ (see Figure 2a). u_b remained constant thereafter. This simulation setup is similar to that of He & Seddighi (2013), though with quantitative differences in the Reynolds number and the amount and rate of the velocity ramp-up.

Simulation parameters for all cases are listed in Table 1. The initial and final steady states are denoted using subscripts "0" and "1", respectively. "SM", "S", and "T" represent the smooth-wall, sandgrain, and a multiscale turbine-blade-roughness cases, respec-

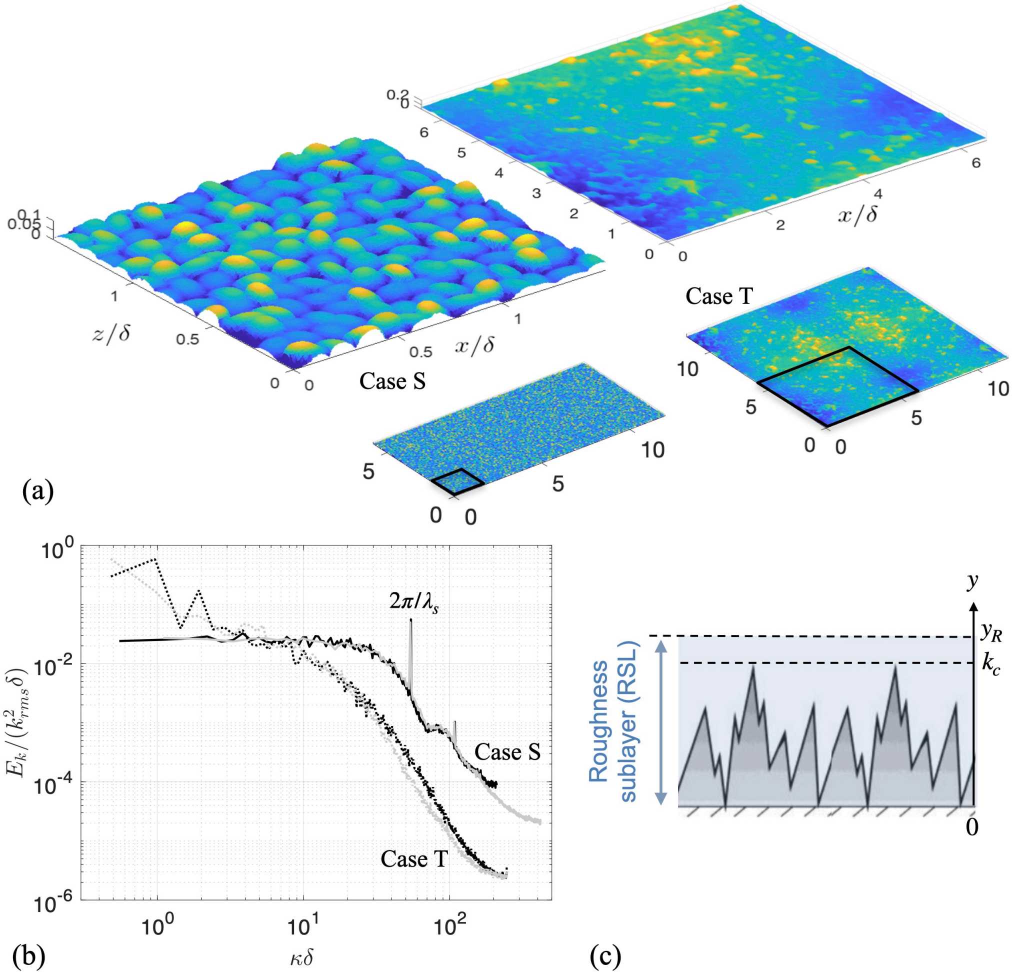

Figure 1: (a) Geometries of sandgrain (case S) and turbine-blade-roughness (case T) surfaces colored by height, with zoomed-in view. (b) Power spectral density of height fluctuations, with wavenumber κ in x (black) and z (gray). (c) Sketch of a rough surface showing various length definitions.

tively. The same time-variation of Re_b was imposed in all cases. Both rough cases started in transitionally rough regime at the initial steady state and became fully rough at the new steady state, as shown by the $k_{s\infty}^+$ values. Here, $k_{s\infty}$ is the equivalent Nikuradse sandgrain height in the fully rough regime of a rough surface; the critical values of $k_{s\infty}^+$ for the present roughnesses corresponding to the lower limit of the fully rough regime were reported by Yuan & Piomelli (2014*a*).

On a rough wall, the wall shear stress τ_w results from both the viscous and pressure drag due to roughness. It was calculated as

$$\tau_w(t) = \frac{\rho}{L_x L_z} \int_{\mathcal{V}} \overline{f}_1(x,y,z,t)\,\mathrm{d}x\,\mathrm{d}y\,\mathrm{d}z + \mu \frac{\partial \langle \overline{u} \rangle_s}{\partial y}\bigg|_{y=0}, \tag{3.1}$$

Surface	R_a/δ	k_c/δ	k_{rms}/R_a	s_k	k_u	ES$_x$	ES$_z$	y_R/k_c
S	0.014	0.09	1.05	0.48	2.97	0.43	0.44	1.10 ± 0.13
T	0.014	0.13	1.17	0.20	3.49	0.10	0.08	1.05 ± 0.10

Table 2: Characteristics of the rough surfaces.

where $f_1(x, y, z, t)$ is the streamwise component of the immersed boundary method body force, $\mathcal{V}$ is the volume of the simulation domain, and L_{x_i} is the domain length in x_i direction. For the two rough surfaces considered herein, the second term on the right-hand-side of Equation (3.1) is negligible. The friction velocity was then obtained as $u_\tau(t) = \sqrt{\tau_w/\rho}$. The corresponding friction Reynolds numbers are tabulated in Table 1; the sandgrain roughness (case S) produced higher wall friction than the multiscale roughness (case T). Grid sizes of the uniform mesh in x and z are shown in wall units in Table 1. In y, the grid is refined near the wall. At the final steady state (i.e. the more critical one for spatial resolution between the two steady states), $\Delta y^+_{\mathrm{min}} < 0.3$ for SM and between 0.6 and 1.7 in the layer below roughness crest for the rough cases.

Two different surfaces roughness, one synthetic sandgrain roughness 'S' and one replicated from a surface scan on a hydraulic turbine blade 'T', are used in the simulations. Figures 1(a) and (b) compare the roughness geometries and the power spectral density of their height fluctuations. Case S shows a prominent spectral peak at the separation length between neighboring grains in x and z, denoted by λ_s, while the T roughness resembles a fractal roughness with a spectral power decay of -2, without a dominant peak at a particular length scale. For further discussion regarding the height power spectral densities, see Mangavelli *et al.* (2021).

Parameters of the two rough surfaces are compared in Table 2. Both surfaces share the same first-order (R_a) and similar second-order moments (k_{rms}) of height statistics, but quite different values of maximum peak-to-trough height (k_c, also called crest height), skewness (s_k) and effective slope (ES) in x or z. Both surfaces are positively skewed (i.e. peaky), with kurtosis values of around 3. Compared to S, the T roughness displays sparser distribution of peaks, leading to a lower skewness value and milder effective slopes. The thickness of the RSL (i.e. y_R, defined as the layer in which $\langle \widetilde{u}^2 \rangle^{1/2}(y)/\langle \overline{u} \rangle(y) > 0.1$) is around 1.1 times of k_c in both cases. y_R varies mildly (within around 10%) throughout the transient process. The domain lengths in x and z are 12δ and 6δ, respectively, for cases SM and S, and both 12δ in case T to accommodate its large in-plane roughness length scales in both x and z. For case S, the spatial resolution of the grain geometry is 8 and 16 points per grain in x and z, respectively. For case T, there is no dominant roughness length scale. The Taylor micro-scale (λ_T) (Yuan & Piomelli 2014*a*; Aghaei Jouybari *et al.* 2021) is thus used to quantify the length of an equivalent roughness element. λ_T is resolved by around 10 points in both x and z.

4. Summary of turbulence statistics

Some observations on flow statistics are summarized here to provide a context for the structural and other analyses reported in Section 5. For comprehensive discussions of the flows, see Mangavelli *et al.* (2021).

Figure 2(a) shows the acceleration of u_b that was imposed in all cases. The friction co-

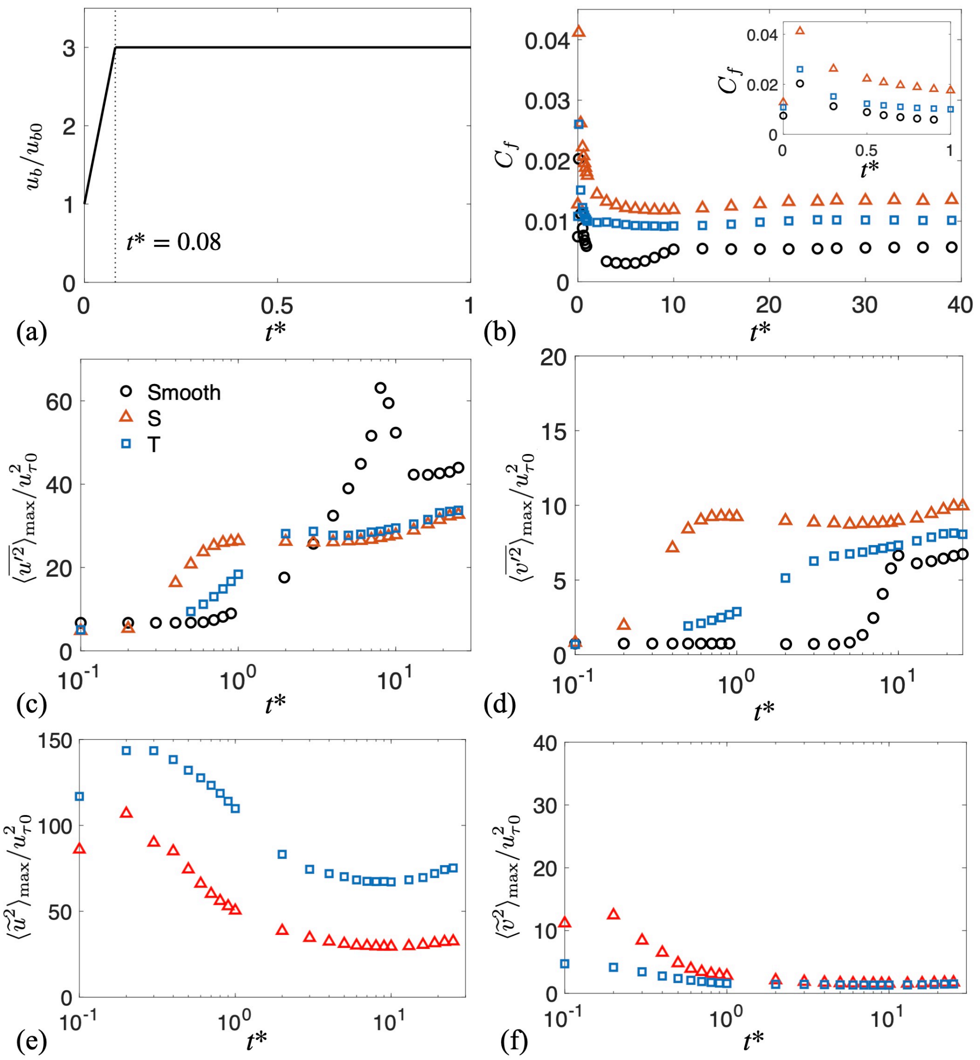

Figure 2: Flow statistics of the transient channels: (a) bulk velocity, (b) friction coefficient, and wall-normal maximum values of streamwise and vertical normal Reynolds stresses (c,d) and form-induced stresses (e,f). (b-f) are reproduced from Mangavelli *et al.* (2021) with permission.

efficient $C_f = 2\tau_w(t)/(\rho u_{b0}^2)$ is compared in Figure 2(b). C_f undergoes a sudden increase for all cases immediately following the u_b ramp-up, and decreases rapidly as the flow starts to recover. Figures 2(c-f) highlight the differences in Reynolds and form-induced stress developments in the three cases.

On the smooth wall, turbulence undergoes reverse transition toward a quasi-laminar state, characterized by a dip of C_f below its long-time value and high Reynolds stress anisotropy (with TKE mostly resting in u'), caused by a delayed response of the TKE redistribution to the acceleration. On the rough walls, however, a clear dip of C_f is absent,

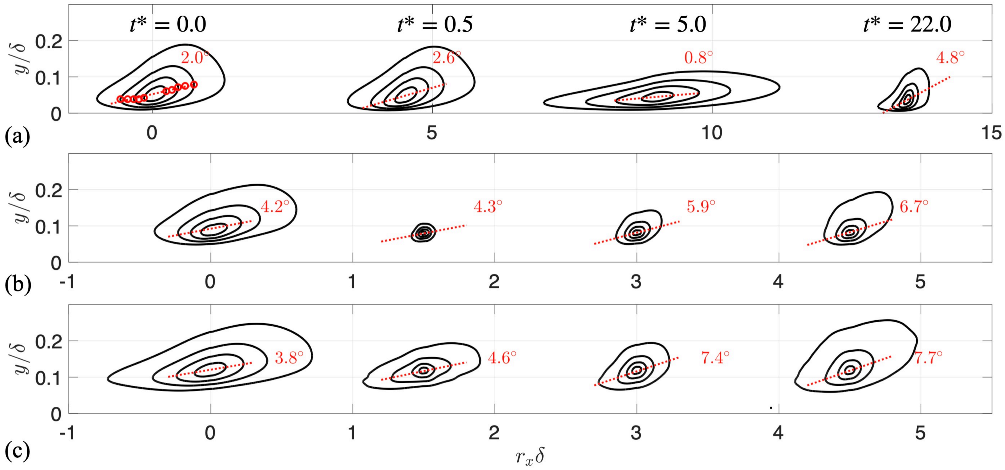

Figure 3: Contours of R_{11} at levels 0.3(0.2)0.9 in Cases SM (a), S (b) and T(c), at four time instances: $t^* = 0.0$, 0.5, 5, and 22. - - - Lines fitted based on outermost points (an example is shown with ○ in (a)) at contour levels 0.5(0.1)0.9, to show inclination angles (marked in red). For clarity, a shift of 4.5 and 1.5 units are used for smooth and rough cases, respectively.

and Reynolds stress anisotropy stays almost unchanged. As opposed to the monotonic increase of u_i' fluctuations to a higher-Reynolds-number state, the $\widetilde{u}_i$ fluctuations display rapid augmentation following the u_b ramp-up and then decrease toward the long-time values. This variation of $\widetilde{u}_i$ intensity was shown to be a result of the variation of $\langle\overline{u}\rangle$ at the edge of the RSL; the ratio between the root-mean-square (RMS) of $\widetilde{u}_i$ and $\langle\overline{u}\rangle(y_R)$ was shown to be almost constant for each rough case.

5. Results

5.1. *Structural characteristics of turbulent velocity*

First, the two-point auto-correlation of the turbulent velocity u_i' centered at an elevation y_{ref} is calculated as

$$R_{11}(r_x, r_y, t) = \frac{\langle\overline{u'(x, y_{ref}, z, t)u'(x + r_x, y_{ref} + r_y, z, t)}\rangle}{\langle\overline{u'^2}\rangle(y_{ref}, t)}, \tag{5.1}$$

where r_x and r_y are separations in streamwise and wall-normal directions, respectively. The intrinsic averaging operator in the nominator on the right-hand-side of Equation (5.1) indicates that only contributions from products with both points ($\vec{x}$ and $\vec{x} + \vec{r}$) in the fluid domain are accounted for in calculating the correlation. Contours of R_{11} in the (x, y) plane are shown in Figures 3 for all cases at $t^* = 0.0$, 0.5, 5, and 22. In the smooth case, the correlation is centered at $y^+_{\text{ref},0} = u_{\tau 0}y_{\text{ref}}/\nu = 10$, which corresponds to the peak elevation of the TKE production at $t^* = 0$, while in the rough cases $y_{\text{ref}}/k_c = 1$, which is near the peak elevations of normal Reynolds stresses (Mangavelli *et al.* 2021). Following Volino *et al.* (2007), the inclination angle θ is calculated using the best fitted line by the linear least square method, based on the points farthest away from the self-correlation point at $(r_x, r_y) = (0, 0)$, both upstream and downstream on the contour lines

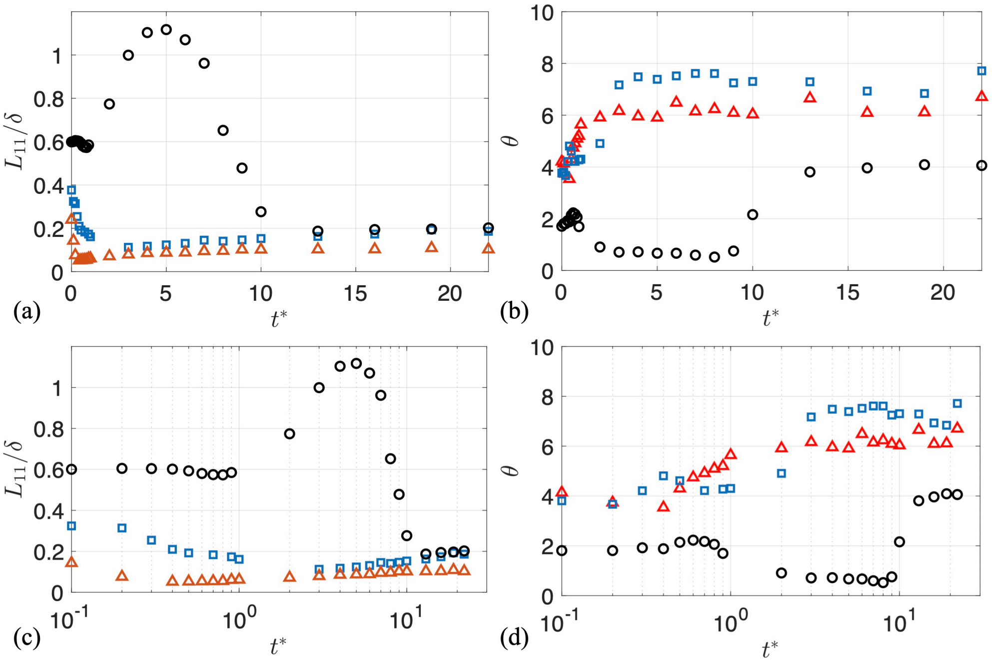

Figure 4: Temporal variation of streamwise integral length (a,c) and inclination angle (b,d) based on R_{11} in SM (○) , S (△), T (□) cases. The correlations are centered at $y^+_{\mathrm{ref},0} = 10$ for SM and $y_{\mathrm{ref}}/k_c = 1$ for S and T. (a,c) show linear scalings of t^* and (c,d) show logarithmic scalings.

with levels from 0.5 to 0.9. These outermost points used for line fitting are shown in the R_{11} contours at $t^* = 0.0$ in Figure 3(a), as an example. The values of θ are listed in the figure. To compare quantitatively the size and inclination of the two-point correlations, Figure 4 shows temporal variations of the streamwise integral length (L_{11}) and θ in all cases. Here, L_{11} is calculated as the integral of R_{11} along r_x from $r_x = 0$ to the r_x value at which R_{11} first decreases below 0.3. A number of y_{ref} elevations (not shown) were used to evaluate the dependencies of both L_{11} and θ on y_{ref}; no significant differences in the comparison among cases and times were observed.

For case SM, in the reverse transition stage (shown at $t^* = 5$), L_{11} increases significantly, accompanied by a much reduced θ, before both quantities recover toward the long-time values at $t^* \approx 13$. The elongation of coherent u' motions (i.e. low speed streaks) was also observed for equilibrium accelerating turbulence such as the sink flow (Yuan & Piomelli 2014*b*) and turbulent boundary layer subjected to FPG (Volino 2020). In both rough cases, on the other hand, L_{11} reduces rapidly, immediately after the step acceleration, reaching a minimum at $t^* \approx 0.4$ for case S and at a later time, $t^* \approx 2.0$, for case T. After then, L_{11} slowly increases toward the long-time values. During this time, an overall monotonic increase of θ is observed on the rough walls. The change in roughness texture only affects quantitative aspects of the large u' motions, but not their trends: the multiscale roughness yields slower variations of both L_{11} and θ following the acceleration at $t^* = 0$.

Now focus on the initial ($t^* = 0$) and late-time states ($t^* = 22$). In the presence of

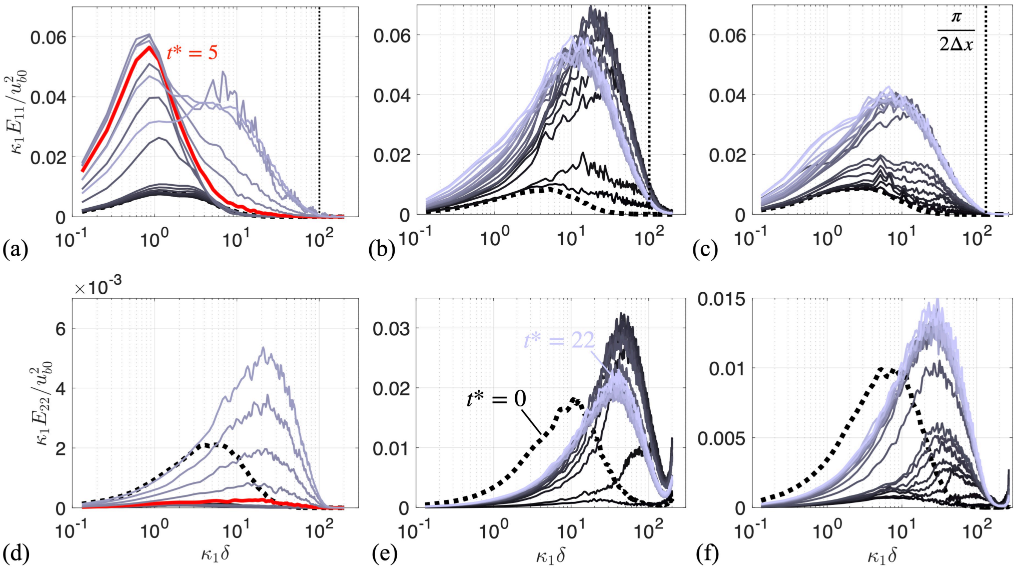

Figure 5: 1D premultiplied power spectra of u' (a-c) and v' (d-f) at $t^* = 0$ (┅) and a series of times (—— , t^* values from 0.1 to 0.9 with step 0.1, from 1 to 9 with step 1, and from 10 to 22 with step 3, lighter colors at later times), in smooth-wall case (a,d) at $y^+ = 10$ and cases S (b,e) and T (c,f) at $y = k_c$. In (d-f), E_{22} at $t^* = 0$ is scaled by a factor of 15 for clarity. In (a-c), ┅ (vertical): highest physically meaningful wavenumber. In (a,d), the profile corresponding to $t^* = 5$ (discussed in text) is highlighted in red.

sandgrain roughness, the x extent is shorter than that in the smooth case at both times. This is because the sandgrain elements are much smaller than δ; it imparts its length scale to the near-wall flow by breaking up long streaky motions near the wall. On the multiscale roughness, however, the initial x extent is closer to that in the sandgrain case, while at late times it approaches the smooth-wall values. This suggests that the streaks are broken up only by the sparsely distributed peaky elements, which are separated by large roughness scales. As the Reynolds number increases after the acceleration, the streaks appear less affected, as the streamwise distances separating the peaky elements approach the order of magnitude of smooth-wall streak lengths, $o(10^3)\delta_\nu$.

To characterize turbulent motions of all sizes, the premultiplied one-dimensional (1D) power spectra ($\kappa_1 E(\kappa_1)$) of u' and v' with streamwise wavenumber $\kappa_1 = 2\pi/\lambda_1$ (where λ_1 is the streamwise wavelength) are shown in Figures 5. First, a remark is given on the DNS spatial resolution, which is deemed sufficient if the wavenumber of the largest energy-containing motions and the highest physically "meaningful" wavenumber are two or more decades apart (Fröhlich *et al.* 2005). The highest meaningful wavenumber is the κ_1 value at which the effective resolution, quantified by an effective wavenumber $\kappa^*_{1,\text{eff}} = \kappa_{1,\text{eff}}\Delta x/\pi$ (Ferziger *et al.* 2002), reaches its maxima. For the present second-order central-difference scheme, the effective wavenumber of the first derivative $\kappa^*_{1,\text{eff}} = \sin(\kappa^*_1\pi)/\pi$ (Ferziger *et al.* 2002) obtains a maximum at $\kappa_1 = \pi/(2\Delta x)$. Since the effective wavenumber drops for κ_1 higher than this value, the simulated fluid motions at scales smaller than $\pi/(2\Delta x)$ are not physically meaningful. Figures 5(a-c) shows that $\pi/(2\Delta x)$ is around two decades higher than the δ scale in all cases, satisfying the criterion of

Fröhlich *et al.* (2005) for DNS spatial resolution.

Figures 5(a,d) show that, for the smooth-wall case, in the reverse-transition phase (e.g. at $t^* = 5$ marked in red) the energy of u' motions is concentrated at large scales of order δ, with only slight changes in the peak location of the v' spectrum. This is consistent with the streamwise elongation of turbulent coherent motions observed in a quasi-laminar flow (Piomelli & Yuan 2013; Yuan & Piomelli 2015). On the other hand, case S (Figures 5 (b,e)) does not show an increase of the low-wavenumber u' content. Instead, the peaks of both u' and v' power spectra shift monotonically toward the dominant length scale of the roughness geometry (i.e. distance between centers of neighboring grains, λ_s, shown in Figure 1(b) as $\kappa\delta \approx 50$). One can infer that the v' associated with the new turbulence generated around the sandgrain roughness has a characteristic streamwise length of the grain separation, and that the u' motions are of lengths two to three times as long, which probably reflects channeling phenomena between grains. In comparison to the sandgrains, the T roughness (Figures 5 (c,f))—characterized by a wide spectrum of length scales up to around 6δ—leads to a large portion of u' being distributed in the scales between $o(\delta)$ and $o(0.1\delta)$ during the transient process. One similarity can be seen between case T and the smooth case: both cases show an amplification of the large-scale u' content at early times (though to a lesser extent in case T), suggesting that, similar to the smooth case, streamwise-elongated eddies are also present around T roughness during the response to acceleration.

5.2. *Time scales of mean-flow strain rates*

The previous section shows that time-variation of the structure of near-wall turbulence depends on the in-plane scales of roughness, with flow over the multiscale T roughness displaying some similarities with that on a smooth wall in terms of velocity coherence length and spectra. Past studies on smooth-wall turbulence attributed the observed streamwise elongation of inclined near-wall turbulent eddies to the stretching due to mean shear, which is quantified using a time-scale ratio (also called "shear rate parameter"), between the turbulence time scale and the time scale of the mean shear. For a transient channel, the time-scale ratio is

$$S^* = \frac{\overline{S}(y,t)\, q^2(y,t)}{2\epsilon(y,t)}, \tag{5.2}$$

where

$$\overline{S}(y,t) = 2(\overline{S}_{ij}\overline{S}_{ij})^{1/2}, \tag{5.3}$$

$$\overline{S}_{ij}(y,t) = \frac{1}{2}\left(\frac{\partial\langle\overline{u}_i\rangle}{\partial x_j} + \frac{\partial\langle\overline{u}_j\rangle}{\partial x_i}\right), \tag{5.4}$$

q^2 is twice the TKE, and ϵ is the TKE dissipation rate. q^2/ϵ represents roughly the time required for the energy of an energy-containing eddy to fully break down to motions in the dissipative subrange through the energy cascade process. Hunt (1978) showed that, for homogeneous turbulence under a strong uniform mean shear, the turbulent eddies are distorted by the mean flow so rapidly that they are simply stretched, other than passing down the effect into smaller-scale eddies through the cascade. In other words, the turbulence time scale is much larger than that of the mean shear, reflected by $S^* \gg 1$. Lee *et al.* (1990) showed that high S^* values between 30 and 40 imposed in initially homogeneous turbulence (without presence of a wall) can produce turbulent velocity and vorticity anisotropies similar to those observed near the wall in a channel flow. Yuan & Piomelli (2015) demonstrated that in the region of quasi-laminar flow in

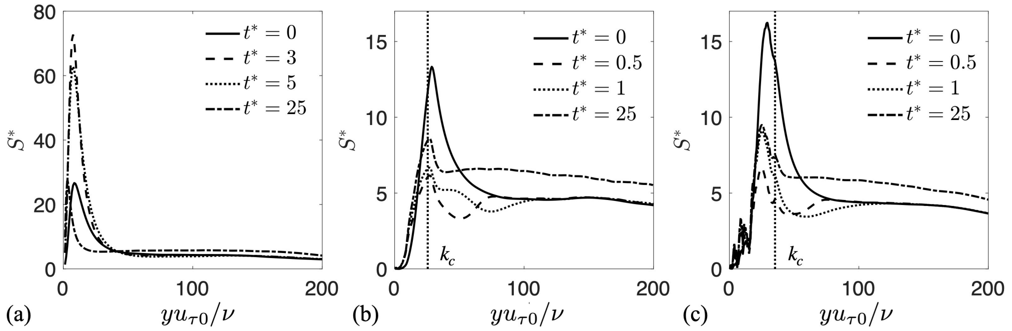

Figure 6: Variation of S^* for (a) SM , (b) S , and (c) T cases in time. In (b) and (c), vertical dotted lines indicate roughness crest height.

a strongly accelerated smooth-wall boundary layer, near-wall S^* values reached up to around 60, compared to a value around only 10 on a rough wall where reverse transition was prevented. In the logarithmic region of the flow, S^* is around 4 to 5, a result of locally equilibrium turbulence.

The y profiles of S^* in all cases are compared in Figure 6. Here, the only non-zero component of the $\overline{S}_{ij}$ tensor is the 12 component, $\partial\langle\overline{u}\rangle/\partial y$. In the smooth case, high magnitudes of S^* near 70 are achieved at $t^* \approx 5$ near the wall, expected for the reverse transition process. In the presence of roughness, the wall-normal peak of $S^*(y)$ occurs near the roughness crest, where the y gradient of $\langle\overline{u}\rangle$ is the strongest. The S^* peak values stay between 5 and 15 throughout the transient, much lower than those in the smooth case, suggesting that the rough-wall DA flow is not strong enough to linearly reshape turbulent eddies. Far from the wall ($y/\delta > 0.1$, or $y^+ > 100$ herein), S^* values are at around 5 at all times, regardless of wall condition. In case T near $y = 0$, one observes significant fluctuations of S^* values. This is probably due to fluctuations in the y-gradient of the roughness geometry function (or fluid area fraction), $\Phi(y)$, in case T, through its involvement in the intrinsic averaging process, $\langle\theta\rangle = 1/(\Phi A_o)\int_{A_f}\theta \mathrm{d}A$ (where A_o is the total planar area). See details of Φ in the Appendix. Using superficial averaging, however, would mask these fluctuations as $\langle\cdot\rangle_s = \Phi\langle\cdot\rangle$ and $\Phi \approx 0$ near the wall.

The discussions above, as well as those in Yuan & Piomelli (2015), focus on the ratio between global (space-averaged) time scales of turbulence and double-averaged mean strain, instead of the local values. However, in rough-wall cases the strongly heterogeneous $\widetilde{u}_i$ inside the RSL may yield local time scale ratios much higher than the global value. In particular, Figure 2 shows that, within a short time after the impulse acceleration (at $t^* \approx 0.3$), the peak of $\langle\widetilde{u}^2\rangle$ reaches one order-of-magnitude higher than that of $\langle\overline{u'^2}\rangle$. This is expected to yield strong local gradients of form-induced velocity inside the RSL, which is quantified next.

We define a time-scale-ratio tensor, S^{*f}_{ij}, to quantify the various strain rate components of $\widetilde{u}_i$. It is similar to the definition of S^*, but based on the form-induced velocity instead of the DA one,

$$S^{*f}_{ij}(y,t) = \left\langle \frac{\widetilde{S}_{ij}\, q^2(x,y,z,t)}{\epsilon(x,y,z,t)} \right\rangle , \tag{5.5}$$

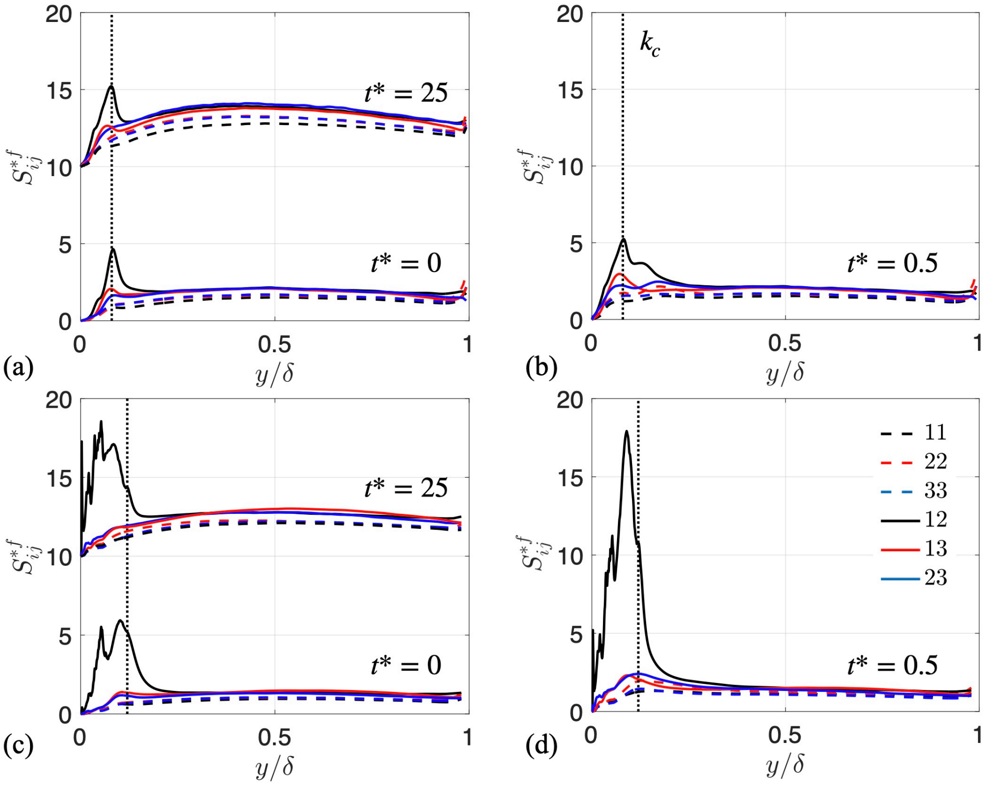

Figure 7: Time-scale ratios of $\widetilde{u}_i$ strain rates for (a-b) S and (c-d) T cases at three times: steady state $t^* = 0$ and long-time state $t^* = 25$ (a,c), as well as a transient state $t^* = 0.5$ (b,d). Profiles corresponding to $t^* = 25$ are offset upward by 10 units for clarify. Vertical dotted lines indicate roughness crest height.

where $\widetilde{S}_{ij}$ is the rate-of-strain tensor of $\widetilde{u}_i$,

$$\widetilde{S}_{ij}(x,y,z,t) = \frac{1}{2}\left(\frac{\partial \widetilde{u}_i}{\partial x_j} + \frac{\partial \widetilde{u}_j}{\partial x_i}\right), \tag{5.6}$$

and the superscript "f" indicates that the time-scale ratio is calculated using the form-induced velocity. Note that, different from the S^* definition in Equation (5.2), local values of three-dimensional ensemble-averaged q^2 and ϵ are used here to evaluate the local time scale ratio. S_{ij}^{*f} components are negligible for the smooth-wall flow.

Wall-normal profiles of all independent components of the S_{ij}^{*f} tensor in both rough cases are compared in Figures 7. Among all, the 12 component is the dominant component for both cases, at all times. Within the 12 component, we found that $\partial\widetilde{u}/\partial y$ is significantly larger than $\partial\widetilde{v}/\partial x$, as $\widetilde{u}$ is the dominant form-induced velocity component. Overall, the plane-averaged form-induced strain rate is similar or weaker compared to the strain rate of $\langle\overline{u_i}\rangle$ during the transient process, with the exception of the 12 component in case T at early stage of the transient (shown at $t^* = 0.5$), which increases to around 18 below the crest elevation. This is roughly 2.5 times the shear rate of $\langle\overline{u_i}\rangle$ at this time (Figure 6c). The higher plane-averaged form-induced time-scale ratio on T roughness than on S can

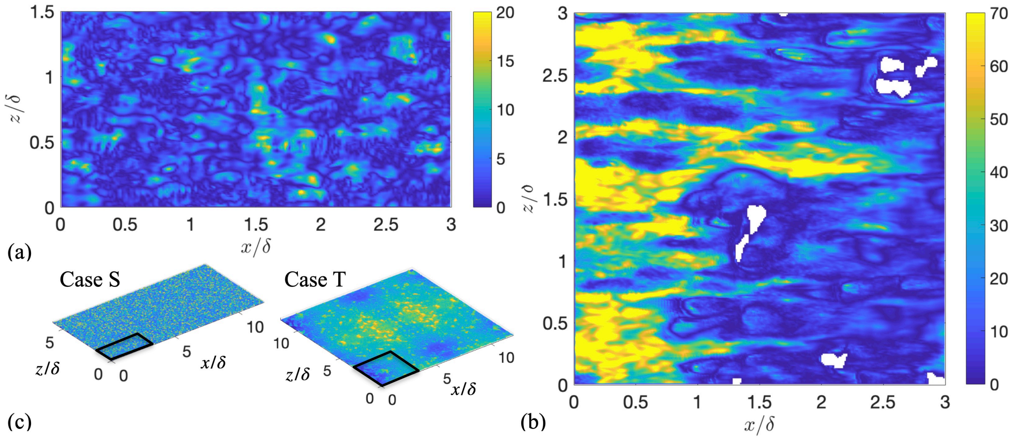

Figure 8: Contours of $\widetilde{S}_{12}q^2/\epsilon$ at $t^* = 0.5$, at respective peak elevations of $S^{*f}_{12}(y)$ profiles for cases S (a, at $y/k_c = 1$) and T (b, at $y/k_c = 0.75$), zoomed in to the regions shown in the full height maps in (c).

be attributed to a stronger $\partial\widetilde{u}/\partial y$, resulting from more intense $\widetilde{u}$ on T roughness than on S (Figure 2e), together with almost identical RSL thicknesses (Table 2). In addition, the comparison between the time-scale ratios at the initial and long-time states ($t^* = 25$) in Fig. 7(a,c) shows that they are similar, with the main difference being slightly higher values of S^{*f}_{ij} of all components in the outer region at $t^* = 25$ than those at $t^* = 0$. This is probably due to more intense high- and low-momentum pathways (as discussed by, for example, Mejia-Alvarez & Christensen (2013) and Womack *et al.* (2022)) in the outer region under the higher Reynolds number. These pathways were discussed, for the present roughnesses and at a Reynolds number similar to the present long-time state, by Yuan & Brereton (2019).

On the T roughness, despite the much lower $\widetilde{u}_i$ strain rates than on the smooth wall in the spatial-average sense as seen by comparing Figures 6(a) and 7(d), locally the time scale ratio can achieve a level similar to that on the smooth-wall, due to heterogeneous nature of this roughness. Figure 8 compares wall-parallel contours of local contribution to S^{*f}_{12} on both rough walls at $t^* = 0.5$. The y elevations of the contours are selected as the respective peak elevations of the average time-scale ratios in the two cases according to Figure 7. Only a portion of the domain is shown for clarity. In case S, local time-scale ratio rarely exceeds 20, and thus the augmented form-induced straining during the transient process acts mainly to promote turbulence production. However, in case T high time-scale ratios are achieved locally in the regions between roughness peaks, with a large area of flow reaching a ratio of 60, similar to the values on a smooth wall.

To quantitatively compare the time-scale ratios in the two rough cases, the cumulative distribution functions (CDF) of $\widetilde{S}_{12}q^2/\epsilon$ in the whole (x, z) domain at the same y elevations are compared in Figure 9. For case T, around 20% of the fluid domain is subject to local time-scale ratios higher than 30 (i.e. level seen in smooth-wall fully developed channels near the wall) and 5% corresponds to ratios higher than 60. Therefore, in the presence of large roughness length scales (with case T as an example), it is possible that strong positive values of $\partial\widetilde{u}/\partial y$ become locally important in early stage of the transient as it leads to streamwise elongation of inclined turbulent eddies (indicated by R_{11} con-

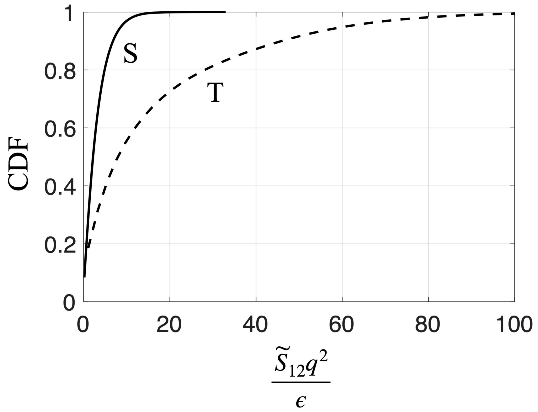

Figure 9: Cumulative distribution functions of local time-scale ratios of $\widetilde{S}_{12}$ shown in Figures 8(a,b).

tours in figure 3c) near the wall. This is consistent with the changes in integral length scale shown in Figure 4 and in the u' spectra shown in Figure 5.

5.3. *Sources of turbulent pressure fluctuations*

Beside the more widely studied form-induced production, we suggested a second mechanism through which the form-induced velocities modify the Reynolds stress balance: indirect augmentation of TKE redistribution (i.e. Π in Equation 1.2) by intensifying turbulent pressure fluctuations, p'. One supporting evidence is that both form-induced velocity intensities and the TKE redistribution to v' through pressure-strain term increase rapidly at early times in the rough cases, as compared to a slow increase of TKE redistribution on a smooth wall (Mangavelli *et al.* 2021).

The following is a selective summary of current understanding of how roughness affects p'. Based on DNS of rough-wall channel flows, Bhaganagar *et al.* (2007) observed that roughness augments pressure fluctuations throughout the boundary layer, and that the RSL thickness defined based on p' RMS was thicker that those based on u_i' or vorticity RMS. Meyers *et al.* (2015) characterized the wall-pressure spectrum and analyzed its scaling based on high-Reynolds-number experimental data. Yang & Wang (2013) showed with large-eddy simulations that roughness geometry and distribution modify wall-pressure fluctuations. Specially, intense pressure fluctuations occur on the front surface of roughness, instead of the back surfaces, suggesting that instantaneous impinging flow structures are more important than vortex shedding to wall-pressure RMS and generation of self noise. Ma *et al.* (2021) examined the two p' source terms that were identified as the dominant ones in fully developed smooth-wall flows: the 12 component of the mean shear term ("MS12" therein) and the 23 component of the turbulent-turbulent term, and concluded that the MS12 term was a more important source between the two on the rough wall. They also explained the links between these terms and local structure of the mean and turbulent velocities.

Due to non-zero $\widetilde{u}_i$ in rough-wall flows, an additional term (represented by $\mathcal{F}$) appears in the Poisson's equation of p',

$$\frac{1}{\rho}\nabla^2 p' = \mathcal{M}(x_i,t) + \mathcal{T}(x_i,t) + \mathcal{F}(x_i,t), \tag{5.7}$$

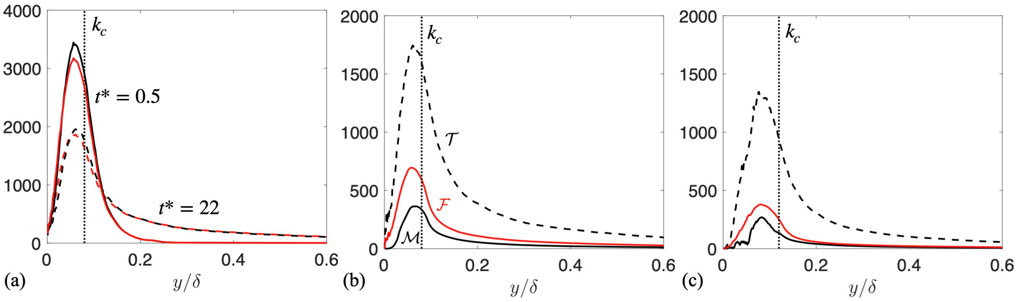

Figure 10: (a) RMS of the left-hand-side (red) and right-hand-side (black) of p' Poisson's equation (Equation 5.7) at $t^* = 0.5$ (——) and 22 (- - -) for case S. (b,c) Steady-state RMS of source terms in cases S (b) and T (c), evaluated at $t^* = 22$. All quantities are normalized using u_{b0} and δ.

where the source terms are

$$\mathcal{M} = -2 \frac{\partial \langle \overline{u_i} \rangle}{\partial x_j} \frac{\partial u'_j}{\partial x_i}, \tag{5.8}$$

$$\mathcal{T} = -\frac{\partial^2}{\partial x_i \partial x_j} \left(u'_i u'_j - \overline{u'_i u'_j} \right), \quad \text{and} \tag{5.9}$$

$$\mathcal{F} = -2 \frac{\partial \widetilde{u}_i}{\partial x_j} \frac{\partial u'_j}{\partial x_i}. \tag{5.10}$$

Here $\mathcal{M}$ is the source due to gradients of double-averaged velocity (i.e. the 'mean shear term'), $\mathcal{T}$ is the turbulent-turbulent term, and $\mathcal{F}$ is the source due to the gradients of $\widetilde{u}_i$. It is unclear how these terms compare, since, to our knowledge, quantitative comparison of all terms has not been reported in the context of rough-wall flows.

In the following, we compare the magnitude of each source term as a function of time, for all cases. First, to estimate the accuracy of the source term calculation in the context of the immersed boundary method, the RMS of the left-hand-side and right-hand-side of Equation (5.7) are compared at various time instances in Figure 10(a), taking case S as an example. The RMS is calculated based on plane averaging using one snapshot at each time (i.e., without ensemble averaging) as $(\cdot)_{\mathrm{rms}} = \langle (\cdot)^2 \rangle_s^{1/2}$, where $(\cdot)$ represents a local instantaneous flow quantity. The difference between the two sides of the equation is shown to be up to 5-8% of the local RMS values. This difference is attributed to discretization error of the finite difference scheme used to calculate the terms in Equation (5.7) and to the exclusion of grid cells that are cut by the fluid-solid interfaces when calculating these terms.

The y-profiles of the RMS of all terms near the new steady state ($t^* = 22$) are compared in Figure 10(b,c) between the two rough cases. Here both ensemble and plane averaging are used in calculating the RMS, obtained as $(\cdot)_{\mathrm{rms}} = \overline{\langle (\cdot)^2 \rangle_s}^{1/2}$. Ma *et al.* (2021) observed that the $\mathcal{M}_{12}$ term is more important than the $\mathcal{T}_{23}$ term, in connection with the presence of maximum $\partial \langle \overline{u} \rangle / \partial y$ inside the RSL and the $\partial v' / \partial x$ augmented by roughness. Surprisingly, the results here show that the least important source is $\mathcal{M}$ in both rough cases, when all components of all term are considered in the calculation. This is probably due to the relatively weak $\partial \langle \overline{u} \rangle_i / \partial x_j$ compared to the form-induced shear $\partial \widetilde{u}_i / \partial x_j$, as well as strong gradients of all u'_i components in the RSL. In addition, $\mathcal{T}$ is

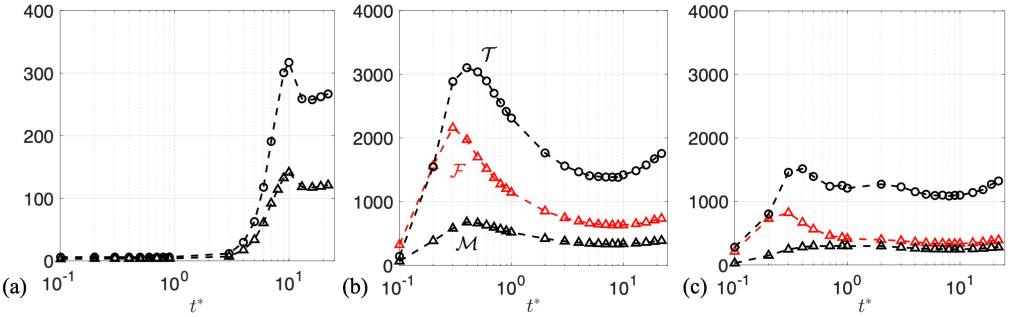

Figure 11: Temporal variations of RMS of p' source terms at their respective wall-normal peak elevations for the smooth case (a) and at $y = 0.7k_c$ for cases S (b) and T (c).

shown here to be the dominant source term regardless of roughness texture. All terms reach a peak slightly below the roughness crest. This is because that the peaks of form-induced stresses (Yuan & Aghaei-Jouybari 2018), Reynolds stresses, and DA mean shear (Raupach *et al.* 1991; Coceal *et al.* 2007; Yang *et al.* 2016) all reach their respective peak values near the roughness crest. In case T, the peaks of the source terms are located lower (toward the middle of the RSL), because of the rarer attainment of the maximum crest height by local roughness peaks due to the presence of large surface scales.

Next, the RMS values of each of the three source terms at a y elevation are evaluated for all times in Figure 11. For the smooth-wall case, as the peak elevations of different terms are not the same and vary with time, the source terms are evaluated at the instantaneous peak location of each term. In the rough-wall cases, however, all terms are evaluated at $y = 0.7k_c$, near the peak elevations of all source terms, independent of time. In the rough cases, the $\mathcal{M}$ term is the least important one not only at steady states, but also during the transient, as turbulence and form-induced velocities in the RSL adjust to the accelerated mean velocity rapidly. All terms increase instantly following the step acceleration on rough walls. Specifically, $\mathcal{F}$ becomes particularly significant in the early stage, due to the intensification of $\widetilde{u}_i$ (Figures 2(e,f)). The $\mathcal{T}$ term increases synchronously with $\mathcal{F}$, probably due to the intensification of TKE associated with stronger form-induced production. On the smooth wall, due to the absence of roughness and $\widetilde{u}_i$, the $\mathcal{T}$ term is not augmented immediately following the bulk acceleration. Instead, the turbulence is "frozen", signified by the persistence of source terms at the initial-state levels till $t^* \approx 3$. The decorrelation between mean flow acceleration and the developments of $\mathcal{M}$ and $\mathcal{T}$ terms were also observed in a smooth-wall boundary layer subject to strong spatial acceleration (Piomelli & Yuan 2013). These results confirm that characteristics of the form-induced velocity as contained in $\mathcal{F}$ are important for the p' evolution. They also suggest that the $\widetilde{u}_i$ distribution determines how turbulence responses to strong acceleration (with more evidence to be shown next).

Spatial distributions of $\mathcal{F}$ and $\mathcal{T}$ terms in both rough cases are compared in Figures 12 and 13, at three time instances: $t^* = 0.1$, $t^* = 0.5$, and $t^* = 10$. In both cases, regions with strong $\mathcal{F}$ and those with strong $\mathcal{T}$ are well correlated at all three time instances, as shown in Table 3 by the single-point cross-correlation between the two sources of values around 0.5 to 0.6. This suggests that early generation of new turbulence depends primarily on form-induced production. In other words, it appears that $\widetilde{u}_i$ strain rates form not just an important source of p', but also the origin of the other important source, $\mathcal{T}$.

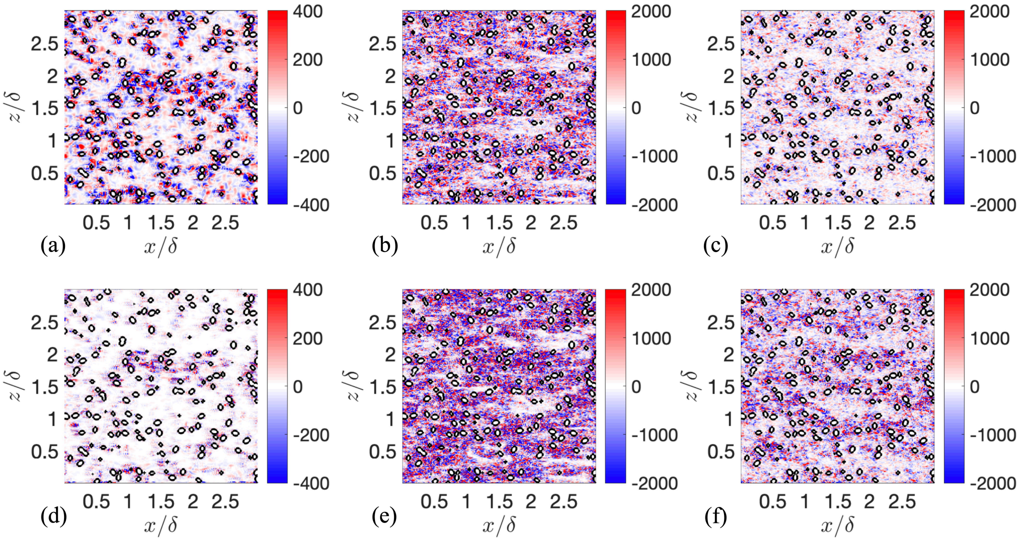

Figure 12: Contours of $\mathcal{F}$ (a-c) and $\mathcal{T}$ (d-f) at $y = 0.7k_c$ for cases S, at $t^* = 0.1$ (a,d), 0.5 (b,e), and 10 (c,f). Black contour lines mark fluid-solid interfaces. All quantities are normalized based on u_{b0} and δ. 1/8 of the domain is shown.

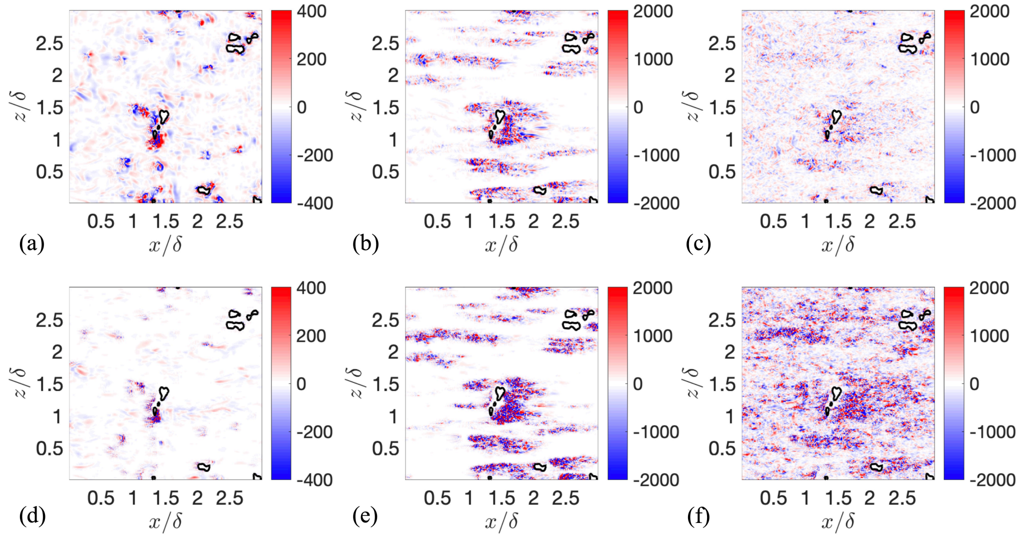

Figure 13: Contours of $\mathcal{F}$ (a-c) and $\mathcal{T}$ (d-f) at $y = 0.7k_c$ for cases T, at $t^* = 0.1$ (a,d), 0.5 (b,e), and 10 (c,f). Black contour lines mark fluid-solid interfaces. All quantities are normalized based on u_{b0} and δ. 1/16 of the domain is shown.

In addition, comparison between Figures 12 and 13 highlights the effect of roughness texture on the rate of increase of p'. First, focus on the largest source term, $\mathcal{T}$. At early times this term takes high magnitudes in the vicinity of peaky roughness elements (e.g. see Figures 12(e) and 13(e)). In case S, the peaky elements associated with the tips of the grains are densely distributed, while in case T the roughness peaks are sparser, separated

Case	$t^* = 0.1$	$t^* = 0.5$	$t^* = 10$
S	0.52	0.56	0.56
T	0.53	0.48	0.50

Table 3: Single-point cross-correlation between $\mathcal{F}$ and $\mathcal{T}$ contours shown in Figs. 12 and 13. The correlation is defined as $\langle|\mathcal{F}| \cdot |\mathcal{T}|\rangle / \left[\langle\mathcal{F}^2\rangle^{1/2} \cdot \langle\mathcal{T}^2\rangle^{1/2}\right]$.

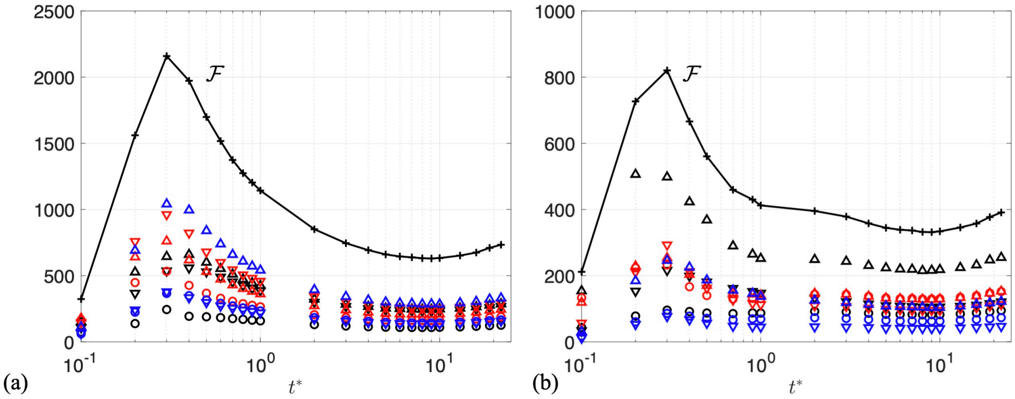

Figure 14: Temporal variations of the RMS of individual terms in $\mathcal{F}$ for cases S (a) and T (b). Symbols: + sum of all terms, ◯ 11, △ 12, ▽ 13, ◯ 21, △ 22, ▽ 23, ◯ 31, △ 32, ▽ 33.

by large roughness scales. As a result, at early times ($0 < t^* < 0.3$) the rate of increase of $\mathcal{T}$ in case T is slower compared to that in case S, as shown in Figure 11. In addition, Figure 11 shows that, in case S, after $\mathcal{F}$ reaches its peak in time at $t^* \approx 0.3$ and starts to decrease toward the steady state, the $\mathcal{T}$ term follows the same trend and decreases from its peak (another evidence of the importance of form-induced production of TKE). In comparison, in case T the $\mathcal{T}$ term displays only a slightly decrease following the decline of $\mathcal{F}$ at $t^* \approx 0.3$. Examination of Figure 13(e,f) explains that this almost constant $\mathcal{T}$ level in case T for $t^* > 0.3$ is due to a combination of both the weakening of local $\mathcal{T}$ values (due to a decrease in $\mathcal{F}$) and the delayed activation of other regions in producing intense turbulent fluctuations.

To further characterize the $\mathcal{F}$ term, individual components $-2(\partial\widetilde{u}_\alpha/\partial x_\beta)(\partial u'_\beta/\partial x_\alpha)$ are compared in Figure 14. For case T, the 12 term $-2(\partial\widetilde{u}/\partial y)(\partial v'/\partial x)$ is significantly higher than other terms at all times. This is because that the large roughness scales induce significant $\widetilde{u}$ in the RSL (Yuan & Aghaei-Jouybari 2018). In case S, however, the 32 and 23 terms are the largest ones, while other terms are also significant. The difference between the two cases highlights the dynamical importance of $\widetilde{v}$ and $\widetilde{w}$ around densely distributed roughness, versus that of $\widetilde{u}$ in the case of a multiscale roughness.

6. Conclusions

This work evaluates various pathways through which the form-induced velocity $\widetilde{u}_i$ affect turbulent flows in equilibrium and non-equilibrium states, based on DNS data of transient turbulent half channels in response to a three-fold step acceleration of bulk velocity at time $t^* = 0$. Two roughness geometries—a densely distributed synthesized sandgrain roughness (case S) and a multiscale turbine-blade roughness (case T)—are imposed on the channel wall; a baseline smooth-wall case (case SM) is also compared. The two roughness geometries share similar first and second moments of roughness height fluctuations, but differ in in-plane scales.

Analyses of two-point turbulent velocity correlations in the transient flow show that, opposed to the smooth-wall cases where energy-containing motions are elongated in x and decrease in inclination angle as signatures of the reverse transition process, on the rough walls the streamwise coherence decreases rapidly after the acceleration and the inclination angle increases sharply. Energy spectra, on the other hand, highlight a difference between the rough cases: while in case S the spectral peaks of u' and v' motions monotonically shift toward characteristic scales of the sandgrains, in case T the u' motions are initial augmented at large scales; the latter suggests local streamwise elongation of velocity streaks similar to the smooth-wall case to some extent.

We show that the dependence of turbulent structure on the in-plane scales of roughness described above may be explained by the local time-scale ratio between the $\widetilde{u}_i$ straining and turbulence. Although both strain rate of double-averaged velocity $\langle\overline{u_i}\rangle$ and the spatial-averaged local strain rate of $\widetilde{u}_i$ yield much smaller time-scale ratios compared to values on a smooth wall, $\widetilde{u}_i$ is shown to give local time-scale ratios above 60 in case T at early times, in large areas between sparse peaks of roughness. These values are similar to the level reached when the turbulence is relaminarized on a smooth wall. This result indicates that, in the presence of in-plane roughness scales of order δ, $\partial\widetilde{u}/\partial y$ may be important during the transient response and result in linear stretching of turbulent eddies.

Besides the additional form-induced production known to be important in transient channel flows (Mangavelli *et al.* 2021), evidence of a second mechanism through which the form-induced velocity indirectly affects the Reynolds stress balance by augmenting p' was presented. We compared all three p' source terms in the roughness sublayer and found that, surprisingly, the least important one at all times is the source due to $\langle\overline{u_i}\rangle$ shear. Both the source due to $\widetilde{u}_i$ gradients and that due to u_i' are important, with the spatial distribution of the latter correlated with the former, probably due to the production of TKE from $\widetilde{u}_i$ shear.

This work provides evidences that the form-induced velocity inside the roughness sublayer is important for turbulence statistics and structure in wall-bounded turbulent flows. $\widetilde{u}_i$ gradients form an important source of p' in an equilibrium flow, while in a non-equilibrium accelerating flow they generate significant amount of TKE in the vicinity of roughness peaks and reshape turbulent eddies in the regions between peaks.

Acknowledgement

The authors gratefully acknowledge the financial support of the Office of Naval Research (Award No. N00014-17-1-2102). Computational support was provided by Michigan State Universitys Institute for Cyber-Enabled Research.

Appendix: Roughness geometry function and its y-gradient

A comparison of $\Phi(y)$ and its gradients between the two rough cases in Fig. 15 shows that the T roughness yields significant fluctuations in $\partial\Phi/\partial y$. This may be due to the

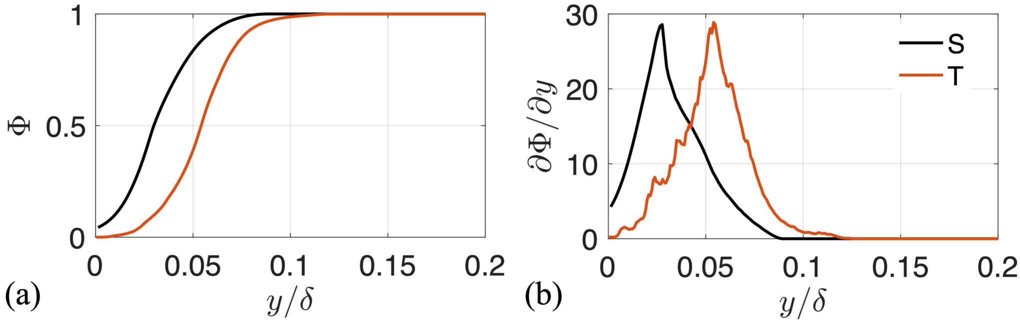

Figure 15: Profiles of roughness geometry functions (a) and its y-gradients (b) in the rough cases.

relatively limited sampling of large in-plane scales of T roughness: only a few δ-scale roughness structures are contained in the simulation domain and, consequently, turbulence statistics are dependent on specific shapes and orientations of these large surface structures. The S roughness, however, consists of around 5000 randomly rotated ellipsoids planted on the wall, producing a smooth $\partial\Phi/\partial y$ profile.

REFERENCES

Aghaei Jouybari, M., Yuan, J., Brereton, G. J. & Murillo, M. S. 2021 Data-driven prediction of the equivalent sand-grain height in rough-wall turbulent flows. *J. Fluid Mech.* **912**, A8–1—23.

Bhaganagar, K., Coleman, G. N. & Kim, J. 2007 Effect of roughness on pressure fluctuations in a turbulent channel flow. *Phys. Fluids* **19**, 028103–1—4.

Bourassa, C. & Thomas, F. O. 2009 An experimental investigation of a highly accelerated turbulent boundary layer. *J. Fluid Mech.* **634**, 359–404.

Cal, R. B., Brzek, B., Johansson, T. & Castillo, L. 2009 The rough favourable pressure gradient turbulent boundary layer. *J. Fluid Mech.* **641**, 129–155.

Chung, D., Hutchins, N., Schultz, M. P. & Flack, K. A. 2021 Predicting the drag of rough surfaces. *Annu. Rev. Fluid Mech.* **53**, 439–471.

Coceal, O., Dobre, A., Thomas, T. G. & Belcher, S. E. 2007 Structure of turbulent flow over regular arrays of cubical roughness. *J. Fluid Mech.* **589**, 375–409.

Devenport, W. J. & Lowe, K. T. 2022 Equilibrium and non-equilibrium turbulent boundary layers. *Progess in Aerospace Sciences* **131**, 100807.

Ferziger, J. H., Perić, M. & Street, R. L. 2002 *Computational methods for fluid dynamics*. Berlin: springer.

Finnigan, J. 2000 Turbulence in plant canopies. *Annu. Rev. Fluid Mech.* **32**, 519–571.

Fröhlich, J., Mellen, C. P., Rodi, W., Temmerman, L. & Leschziner, M. A. 2005 Highly resolved large-eddy simulation of separated flow in a channel with streamwise periodic constrictions. *J. Fluid Mech.* **526**, 19–66.

Ghodke, C. D. & Apte, S. V. 2016 DNS study of particle-bed–turbulence interactions in an oscillatory wall-bounded flow. *J. Fluid Mech.* **792**, 232–251.

He, S. & Seddighi, M. 2013 Turbulence in transient channel flow. *J. Fluid Mech.* **715**, 60–102.

HUNT, J. C. R. 1978 A review of the theory of rapidly distorted turbulent flows and its applications. *Fluid Dyn. Trans* **9**, 121–152.

JELLY, T. O. & BUSSE, A. 2019 Reynolds number dependence of Reynolds and dispersive stresses in turbulent channel flow past irregular near-Gaussian roughness. *Int. J. Heat Fluid Flow* **80**, 108485.

JIMÉNEZ, J. 2004 Turbulent flows over rough walls. *Annu. Rev. Fluid Mech.* **36**, 173–196.

LEE, M. J., KIM, J. & MOIN, P. 1990 Structure of turbulence at high shear rate. *J. Fluid Mech.* **216**, 561–583.

MA, R., ALAMÉ, K. & MAHESH, K. 2021 Direct numerical simulation of turbulent channel flow over random rough surfaces. *J. Fluid Mech.* **908**, A40.

MANGAVELLI, S. C., YUAN, J. & BRERETON, G. J. 2021 Effects of surface roughness topography in transient channel flows. *J. Turbul.* **22**, 434–460.

MEJIA-ALVAREZ, R. & CHRISTENSEN, K. T. 2013 Wall-parallel stereo particle-image velocimetry measurements in the roughness sublayer of turbulent flow overlying highly irregular roughness. *Phys. Fluids* **25**, 115109–1–24.

MEYERS, T., FOREST, J. B. & DEVENPORT, W. J. 2015 The wall-pressure spectrum of high-Reynolds-number turbulent boundary-layer flows over rough surfaces. *J. Fluid Mech.* (768), 261–293.

MIGNOT, E., BARTHELEEMY, E. & HURTHER, D. 2009 Double-averaging analysis and local flow characterization of near-bed turbulence in gravel-bed channel flows. *J. Fluid Mech.* **618**, 279–303.

NARASIMHA, R. & SREENIVASAN, K. R. 1973 Relaminarization in highly accelerated turbulent boundary layers. *J. Fluid Mech.* **61**, 417–447.

NIKORA, V., GORING, D., MCEWAN, I. & GRIFFITHS, G. 2001 Spatially averaged open-channel flow over rough bed. *J. Hydr. Engng* **127**, 123–133.

PIOMELLI, U. & YUAN, J. 2013 Numerical simulations of spatially developing, accelerating boundary layers. *Phys. Fluids* **25**, 101304–1—21.

POKRAJAC, D., CAMPBELL, L. J., NIKORA, V. & MANES, C. ADN MCEWAN, I. 2007 Quadrant analysis of persistent spatial velocity perturbations over square-bar roughness. *Exp. Fluids* **42**, 413–423.

RAUPACH, M. R., ANTONIA, R. A. & RAJAGOPALAN, S. 1991 Rough-wall boundary layers. *Appl. Mech. Rev.* **44**, 1–25.

RAUPACH, M. R. & SHAW, R. H. 1982 Averaging procedures for flow within vegetation canopies. *Bound.-Lay. Meteorol.* **22**, 79–90.

SEDDIGHI, M., HE, S., POKRAJAC, D., O'DONOGHUE, T. & VARDY, A. E. 2015 Turbulence in a transient channel flow with a wall of pyramid roughness. *J. Fluid Mech.* **781**, 226–260.

VOLINO, R. J. 2020 Non-equilibrium development in turbulent boundary layers with changing pressure gradients. *J. Fluid Mech.* **897**, A2–1–48.

VOLINO, R. J., DEVENPORT, W. J. & PIOMELLI, U. 2022 Questions on the effects of roughness and its analysis in non-equilibrium flows. AIAA Paper 2022-0695.

VOLINO, R. J., SCHULTZ, M. P. & FLACK, K. A. 2007 Turbulence structure in rough- and smooth-wall boundary layers. *J. Fluid Mech.* **592**, 263–293.

WILSON, N. R. & SHAW, R. H. 1977 A higher order closure model for canopy flow. *J. Appl. Meteor.* **16**, 1197–1205.

WOMACK, K. M., VOLINO, R. J., MENEVEAU, C. & SCHULTZ, M. P. 2022 Turbulent boundary layer flow over regularly and irregularly arranged truncated cone surfaces. *J. Fluid Mech.* **933**, A38.

Yang, Q. & Wang, M. 2013 Boundary-layer noise induced by arrays of roughness elements. *J. Fluid Mech.* **727**, 282–317.

Yang, X., Sadique, J., Mittal, R. & Meneveau, C. 2016 Exponential roughness layer and analytical model for turbulent boundary layer flow over rectangular-prism roughness elements. *J. Fluid Mech.* **789**, 127–165.

Yuan, J. & Aghaei-Jouybari, M. 2018 Topographical effects of roughness on turbulence statistics in roughness sublayer. *Phys. Rev. Fluids* **3**, 114603.

Yuan, J. & Brereton, G. J. 2019 Structure of turbulent flows on heterogeneous irregular rough surfaces. In *Proceedings of 11th International Symposium of Turbulence and Shear Flow Phenomena (TSFP-11)*.

Yuan, J. & Piomelli, U. 2014*a* Estimation and prediction of the roughness function on realistic surfaces. *J. Turbul.* **15**, 350–365.

Yuan, J. & Piomelli, U. 2014*b* Numerical simulations of sink-flow boundary layers over rough surfaces. *Phys. Fluids* **26**, 015113–1—015113–28.

Yuan, J. & Piomelli, U. 2014*c* Roughness effects on the Reynolds stress budgets in near-wall turbulence. *J. Fluid Mech.* **760**, R1.

Yuan, J. & Piomelli, U. 2015 Numerical simulation of a spatially developing accelerating boundary layer over roughness. *J. Fluid Mech.* **780**, 192–214.